Stimulated raman adiabatic passage in optomechanics

Fedoseev, V.

3

STIRAP of a classical state

In multimode optomechanical systems, the mechanical modes can be coupled via the radiation pressure of the common optical mode, but the fidelity of the state transfer is limited by the optical cavity decay. In this chapter we demonstrate stimulated Raman adiabatic passage (STIRAP) in optomechanics, where the optical mode is not populated during the coherent state transfer between the mechanical modes. Therefore the optical decay channel is avoided. We show a state transfer of a coherent mechanical excitation between vibrational modes of a membrane in a high-finesse optical cavity with a transfer efficiency of 86%. Combined with exceptionally high mechanical quality factors, STIRAP between mechanical modes can enable generation, storage and manipulation of long-lived mechanical quantum states, which is important for quantum information science and for the investigation of macroscopic quantum superpositions.

This chapter is based on: **V. Fedoseev**, F. Luna, I. Hedgepeth, W. Löffler and D. Bouwmeester, Stimulated Raman Adiabatic Passage in Optomechanics, Phys. Rev. Lett. 126, 113601 (2021).

3.1 Introduction

STIRAP describes adiabatic population transfer between two states coherently coupled via a mediating state that remains unoccupied. This renders STIRAP robust against loss and noise in the mediating state, leading to profound applications in atomic- and molecular-optics research [16, 36], trapped-ion physics [37], superconducting circuits [38], other solid-state systems [39, 40], optics [41], in entanglement generation [42, 43] and qubit operations [44]. STIRAP in optomechanics has been proposed for optical frequency conversion with a mechanical mode being the mediating state, where the fidelity of the state transfer is not deteriorated by the residual thermal noise of the mechanical mode [45, 46], and for a mechanical state transfer through the common optical mode [47].

In a theory paper [48] a method was proposed to create an indirect coupling

between non-degenerate mechanical modes via a common optical mode. In this scheme the coupling is created by two stationary red-detuned pump light fields. Experimentally the coupling was observed in an electromechanical system via splitting of the hybridized mechanical peaks in the avoided level crossing [49]. The same indirect coupling can be seen in the energy transfer between two mechanical modes. Such a transfer between the two non-degenerate mechanical modes was demonstrated in [12, 15] where the beating between two driving light fields bridges the frequency difference of the modes. The motion of the modes modulate the intracavity light fields creating motional sidebands [9]. This transfer scheme relies on the matched motional sidebands and requires the detuning of the driving fields to be much higher than the mechanical frequencies [48]. In this case the other unmatched motional sidebands are of similar amplitudes as the matched ones and cause incoherent driving or cooling of the mechanical modes, limiting the state transfer fidelity. In optomechanical STIRAP in the sideband-resolved regime the loss due to the unmatched motional sidebands can be made negligibly small by choosing the detuning of the two driving light fields equal to the frequencies of the mechanical modes. In this case the two matched sidebands at the cavity resonance interfere destructively driving the state transfer. The other motional sidebands have much smaller amplitudes. This strongly decreases the unwanted effects of the unmatched motional sidebands and allows the state transfer fidelity to approach unity in the quantum regime. Such a state transfer is equivalent to the π-pulse (π rotation on the Bloch-sphere in the vertical plane). Via a specific modification of the STIRAP driving pulses a $\pi/2$-pulse can be achieved resulting in a fully entangled state. In spite of the two red-detuned pumps no energy is lost to the environment from the mechanical modes in a STIRAP transfer with the adiabaticity condition fulfilled.

An indirect cavity-mediated coupling can also be created via one red-detuned pump and one blue-detuned pump with detunings equal to the corresponding frequencies of the mechanical modes. Such a scheme was realized in electro-mechanical systems in the quantum regime [50, 51, 52]. The coupling resulted in an entanglement of the two mechanical oscillators. In this scheme the state of the mechanical mode corresponding to the red-detuned pump (mode 1) is transferred to the other mechanical mode (mode 2) similar to the two red-detuned pumps scheme. But, in addition, mode 2 is being driven incoherently by the blue-detuned pump and a fully entangled state cannot be achieved.

Fig. 3.1(a) shows the basic Λ-type arrangement of 3 levels typical for STIRAP. In the triply rotating frame at frequencies $\omega_i = E_i/\hbar$ for states ψ_i, $i = 1, 2, 3$, the Hamiltonian is:

$$\hat{H}(t) = \frac{\hbar}{2}\begin{pmatrix} 0 & \Omega_{12}(t) & 0 \\ \Omega_{12}(t) & 0 & \Omega_{23}(t) \\ 0 & \Omega_{23}(t) & 0 \end{pmatrix}, \tag{3.1}$$

with Ω_{12} and Ω_{23} the Rabi frequencies resulting from two driving fields at frequencies $(E_2 - E_1)/\hbar$ and $(E_2 - E_3)/\hbar$. One of the three instantaneous eigenstates has eigenvalue 0 and does only include states ψ_1 and ψ_3:

$$\Phi_0(t) = \cos\theta(t)\psi_1 - \sin\theta(t)\psi_3, \tag{3.2}$$

with $\tan\theta(t) = \Omega_{12}(t)/\Omega_{23}(t)$. The existence of this "dark" state in optomechanics

has been firstly demonstrated in [53]. STIRAP is based on the adiabatic following of $\Phi_0(t)$ by slowly varying $\theta(t)$ from $\theta(-\infty) = 0$ to $\theta(\infty) = \pi/2$. Thus, the system can be adiabatically transferred from ψ_1 to ψ_3, never occupying state ψ_2. Fig. 3.1(b) shows a driving pulse sequence satisfying this requirement and Fig. 3.1(c) shows the energy eigenvalues corresponding to the three eigenstates $\Phi_+(t)$, $\Phi_0(t)$, and $\Phi_-(t)$. This driving pulse sequence together with the adiabaticity condition $\sqrt{\Omega_{12}(t)^2 + \Omega_{23}(t)^2} \gg \dot{\theta}$ prevents the lossy mediating state from being occupied throughout the transfer process.

The Hamiltonian in Eq. (3.1) can be realized in multimode optomechanics [45, 46] where states 1 and 3 are mechanical excitations with frequencies ω_1 and ω_2 and state 2 is an optical cavity mode at $\omega_{\rm cav}$, see Fig. 3.1(d). Two optical driving fields at $\omega_{{\rm L}i} = \omega_{\rm cav} - \omega_i$ for $i = 1, 2$ are introduced in order to create the beamsplitter interaction $\hat{a}\hat{b}_i^\dagger + \hat{a}^\dagger\hat{b}_i$ that couples the mechanical modes to the cavity mode, where $\hat{a}(\hat{a}^\dagger)$ and $\hat{b}_i(\hat{b}_i^\dagger)$ are the photon and phonon annihilation (creation) operators.

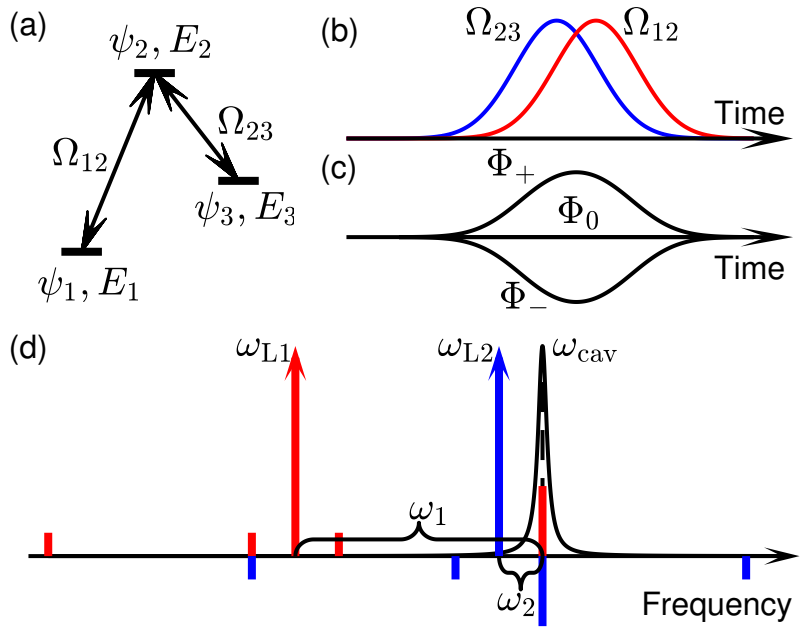

Figure 3.1: STIRAP scheme in optomechanics. (a) Energy levels diagram. (b) Coupling strengths of the pulse sequence for the driving fields. (c) The resulting energy eigenvalues for the instantaneous Hamiltonian eigenstates. STIRAP explores the properties of $\Phi_0(t)$ given in Eq. (3.2). (d) The optomechanical implementation contains a cavity mode at frequency $\omega_{\rm cav}$, two driving fields at $\omega_{\rm L1}$ and $\omega_{\rm L2}$ and eight motional sidebands due to the mechanical modes at ω_1 and ω_2 on the driving fields, red bars corresponding to the sidebands on $\omega_{\rm L1}$ and blue bars corresponding to the sidebands on $\omega_{\rm L2}$. Two sidebands match $\omega_{\rm cav}$. In the case of $\Phi_0(t)$ the states ψ_1 and ψ_3 are out of phase leading to destructive interference of the sidebands that overlap with $\omega_{\rm cav}$.

The optical mode can be represented by the operator $\hat{a} = \bar{\alpha} + \delta\hat{a}$, where $\bar{\alpha}$ is the

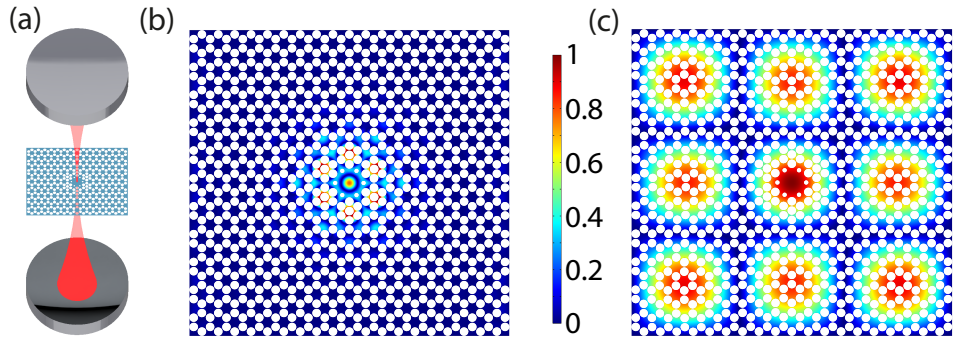

Figure 3.2: Optomechanical setup. (a) A transparent dielectric membrane patterned with a phononic crystal is placed in the middle of a high-finesse optical cavity. Shift of the membrane along the axis of the cavity changes the cavity resonance frequency, causing coupling of light in the cavity to vibrational modes of the membrane. (b) Simulated displacement of a mechanical mode of the defect of the phononic crystal. The mode is localized as its frequency lies in the band gap (mode 1, initially excited). (c) Simulated displacement of the 3,3 drumhead mode of the full membrane (mode 2). This second mode was selected because it has an appropriate mechanical frequency and quality factor and has a maximum amplitude at the center. This allows both modes to be aligned for optimal coupling to the same cavity mode.

average coherent amplitude due to the driving optical fields and $\delta\hat{a}$ is the fluctuating term [9]. Each mechanical mode produces two sidebands on each optical field. Due to resonance with the cavity the two sidebands with frequencies ω_{cav} acquire much larger amplitudes than the other sidebands. Taking into account only those two sidebands and including mechanical and optical loss rates, Γ_i and κ, the time evolution of the state vector $\psi(t) = (\hat{b}_1(t), \delta\hat{a}(t), \hat{b}_2(t))^T$ is given by

$$i\frac{d\psi(t)}{dt} = \begin{pmatrix} -i\frac{\Gamma_1}{2} & g_1(t) & 0 \\ g_1(t) & -i\frac{\kappa}{2} & g_2(t) \\ 0 & g_2(t) & -i\frac{\Gamma_2}{2} \end{pmatrix} \psi(t). \tag{3.3}$$

Here, the rotating wave approximation has been used and it is valid in the linearized regime of cavity optomechanics [9]. $g_i(t)$ is the optomechanical multiphoton coupling for mechanical modes $i = 1, 2$, $g_i = g_{i0}\bar{\alpha}_i$, where g_{i0} is single photon coupling and $\bar{\alpha}_i$ is the driving field at $\omega_{\mathrm{L}i}$, see section Theory. Equation (3.3) is valid in the sideband resolved regime together with the requirement $|\omega_1 - \omega_2| \gg \kappa$ and is identical to Eq. (3.1) in the absence of losses and with the Rabi frequencies Ω_{12} and Ω_{23} corresponding to $2g_1$ and $2g_2$.

Experimentally we demonstrate the state transfer in the membrane-in-the-middle (MIM) configuration [54], where a membrane with low optical absorption is placed in the center of a high-finesse optical cavity with $\kappa/2\pi = 54$ kHz (including membrane), see Fig. 3.2. A displacement of the membrane along the optical axis leads to a shift in the optical cavity transmission described by the interaction Hamiltonian $\hat{H}_{int} = -\hbar g_0 \hat{a}^\dagger \hat{a}(\hat{b} + \hat{b}^\dagger)$, where g_0 is the single photon optomechanical coupling [9]. The membrane is a highly stressed 25 nm thick SiN film lithographically patterned

with a phononic crystal with a defect in its center suspended on a silicon frame [7]. There are two types of mechanical modes: whole membrane drumhead modes and modes localized near the phononic crystal defect with frequencies in the phononic crystal bandgap. Vibrational energy of the drumhead modes is mainly lost in the bending regions where the membrane is connected to the frame [55, 7]. The modes localized near the defect possess enhanced quality factors by 1-2 orders of magnitude compared to the drumhead modes [7]. We demonstrate STIRAP between the fundamental mode of the defect with frequency $\omega_1/2\pi = 1.25$ MHz and quality factor $Q = 1.3 \cdot 10^7$ (mode 1, Fig. 3.2(b)), and the 3,3 drumhead mode with $\omega_2/2\pi = 0.22$ MHz and $Q = 1.2 \cdot 10^6$ (mode 2, Fig. 3.2(c)). The modes are coupled to the optical cavity with single-photon couplings of $g_{01}/2\pi = 1.5 \pm 0.1$ Hz and $g_{02}/2\pi = 1.0 \pm 0.1$ Hz respectively. In addition to these modes possessing relatively large single photon coupling, quality factors and frequency separation, there are no other mechanical modes in the range of $\sim 1/\sigma$ from ω_1 and ω_2, where σ defines the width of the driving pulses. The latter requirement guaranties that modes 1 and 2 are not coupled to other modes during the transfer. STIRAP is very sensitive to the double-photon detuning $\Delta_{2\mathrm{ph}} = (\omega_{\mathrm{L1}} + \omega_1) - (\omega_{\mathrm{L2}} + \omega_2)$ [13], therefore the two optical fields are created by amplitude modulation of light from a single 1064 nm laser using acousto-optic modulator (AOM). As a result the laser phase noise is not limiting the transfer efficiency [56]. Due to nonlinear response of the AOM the detuning of this single laser light tone is chosen such that harmonics of the AC voltage sent to the AOM have a negligible effect on the transfer efficiency (see section Generation of driving pulses). The membrane is in a vacuum chamber with pressure below 10^{-6} mbar at room temperature.

3.2 Experimental details

3.2.1 Setup

The motion of the membrane is read out via the light fields generated by a probe laser at ω_{probe} (10 μW) locked to the transmission resonance frequency of the optical cavity via the Pound-Drever-Hall technique (PDH) [34]. In order to measure the instantaneous oscillation displacement of a mechanical mode ω, the reflection signal is demodulated at $\omega + \omega_{\mathrm{EOM}}$, where $\omega_{\mathrm{EOM}} = 10$ MHz is the detuning frequency of the sidebands in the PDH locking scheme. The driving light fields generated by the pump laser at ω_{pump} is locked to the probe laser by a phase-locked loop, see Fig. 3.3. The light fields from the two lasers are measured by a fast photodetector and the beating signal is mixed with a reference microwave signal, supplied by an RF generator. The resulting signal is sent to a proportional-integral-differential controller (PID) which adjusts the frequency of the pump laser. The difference between the lasers frequencies is kept at $\omega_{\mathrm{probe}} - \omega_{\mathrm{pump}} = 2\mathrm{FSR} + \Delta \sim 3$ GHz because the dispersion curves of membrane-in-the-middle systems are parallel for all odd and all even resonances [18]. This ensures a well-defined cavity resonance detuning of the pump laser in spite of drifts in the membrane position along the optical axis (~ 10 nm/hour). The pump light fields have orthogonal polarization to the probe light fields in order to minimize interference of both fields at the reflection photodetector.

To excite a membrane mechanical mode, an AC voltage (~ 10 mV) at its mechanical frequency is applied to a needle placed close to the defect of the membrane (~ 0.5 mm). The full membrane 1,1 mechanical mode thermal motion is damped by applying an electrostatic force through the needle. The force is proportional to the instantaneous position of this mode but delayed by a quarter of its oscillation, which effectively creates a frictional force proportional to the mode's velocity.

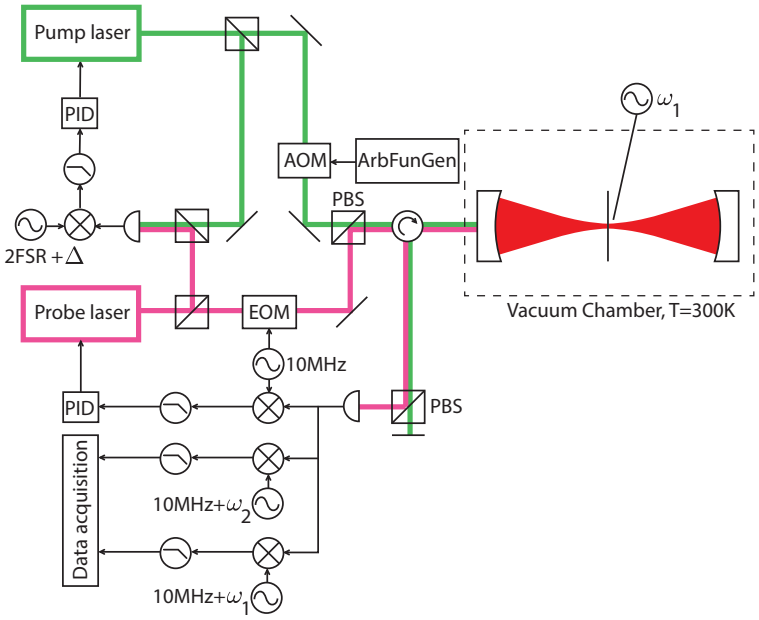

Figure 3.3: Optical setup. The probe laser is locked to the transmission peak of the cavity. The pump laser is locked to the probe laser with frequency difference $\omega_{\mathrm{probe}} - \omega_{\mathrm{pump}} = 2\mathrm{FSR} + \Delta$, controlled by an RF source. The driving pulses are shaped by electronic pulses sent to the AOM from an arbitrary wave function generator (ArbFunGen). Polarizing beam splitters (PBS) are used to separate the probe and pump light fields. Mechanical modes are excited by a needle placed close to the membrane defect.

3.2.2 Membrane positioning

The dispersion curves of a membrane-in-the-middle system are parallel for the curves separated by 2FSR provided the membrane is positioned exactly in the middle of the cavity. For a small displacement z of the membrane from the center, the free-spectral range changes as $2\mathrm{FSR} - 2\mathrm{FSR}_{\mathrm{middle}} \propto 2\mathrm{FSR}_{\mathrm{middle}} \frac{z}{L} \sin \pi \frac{z}{\lambda}$, where L is the length of the cavity and λ is the wavelength. The membrane holder is mounted on a tip-tilt stage with 3 vacuum compatible motors (1 step ~ 20 nm). To minimize the influence of the membrane drift along the optical axis, the membrane was moved towards the middle of the cavity to $z \sim 30$ μm by measuring 2FSR as a function of z, which

provides an estimate for the direction and amplitude of the movement. To further minimize the influence of membrane drifts, we use a piezo element to bring the membrane to the position where 2FSR has a local maximum as a function z. This position coincides with the maximum optomechanical coupling strength. As a result an average drift of the membrane during a measurement run of 1 hour causes an acceptable change of 2FSR ~ 5 kHz. When the actual experiment is running, we use the piezo to bring the membrane back to the position of maximum 2FSR every hour.

3.2.3 Membrane fabrication

We begin the fabrication process of the devices with a commercially supplied $525\ \mu\mathrm{m}$ thick silicon wafer coated on both sides with 25 nm of LPCVD high-stress silicon nitride. We pattern the phononic crystal structure into the nitride on one side through the use of standard photolithography. During a second photolithography step, we use an IR contact aligner to pattern a square hole in photoresist on the opposite side of the chip. A subsequent Bosch etch step etches through the exposed nitride and removes about $425\ \mu\mathrm{m}$ of the silicon underneath the phononic crystal. After cleaning the chip in piranha solution, we release the phononic crystal membrane by wet etching the remaining $100\ \mu\mathrm{m}$ of silicon using KOH at $80°$C. We perform a final clean by submerging the chip in HF for 1 minute and then we extract it out of IPA and allow it to dry through evaporation.

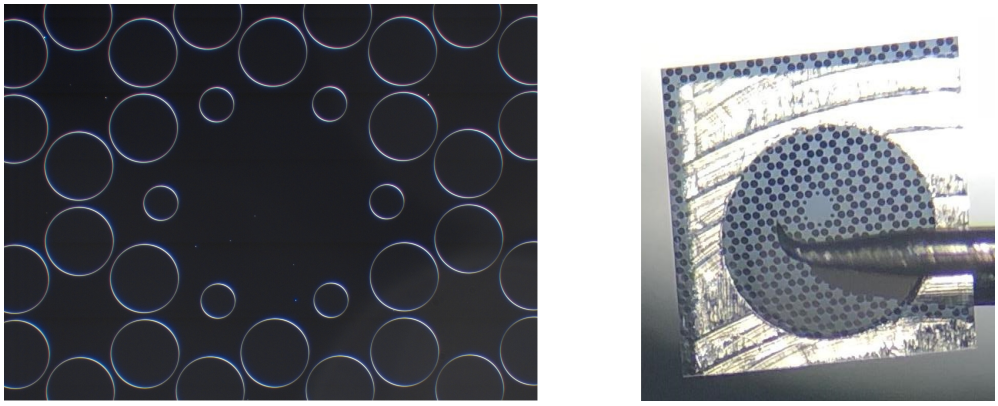

Figure 3.4: Photos of the membrane. The left photo is the dark field imaging, any particle on the membrane is visible as a bright spot. The right photo shows the device on a metallic holder. The sharp metallic tip for driving via electrostatic forces is also visible in the front.

3.2.4 Generation of driving pulses

Fluctuations in the difference of the frequencies of the two driving pulses must be much less than $1/T_{\mathrm{transfer}}$ for the adiabaticity condition to be satisfied[13]. We achieve this by generating both driving pulses from the same pump laser by frequency shift, see Fig. 3.5. An AC voltage with frequency ω_{AOM} generates two light

fields in the first diffraction maximum of the acousto-optical modulator (AOM) with frequencies $\omega_{\mathrm{pump}} \pm \omega_{\mathrm{AOM}}$. In order to independently address both frequencies required for the state transfer (ω_{L1} and ω_{L2}), we send two electronic pulses to the AOM with frequencies $\omega_{\mathrm{AOM},i}$, $i = 1, 2$ and Gaussian envelopes generated by an arbitrary function generator (ArbFunGen). The pump laser detuning $\Delta = 3.5$ MHz is chosen so that $\omega_{\mathrm{L}i} = \omega_{\mathrm{pump}} + \omega_{\mathrm{AOM},i} = \omega_{\mathrm{cav}} - \omega_i$ for mechanical modes at ω_i, $i = 1, 2$, and the effect on the transfer process of the other pair of light fields at $\omega_{\mathrm{pump}} - \omega_{\mathrm{AOM},i}$ and harmonics $\omega_{\mathrm{pump}} + k \cdot \omega_{\mathrm{AOM},i}$, $k = 2, 3, 4, ...$ is negligible. The measured amplitude of the 2^{nd} harmonics is much smaller than that of the 3^{rd} harmonics, as is represented by the arrows labeled "harm." in Fig. 3.5. To check the effect of the harmonics, we excite the mechanical modes to a level much higher than the thermal motion and we send driving pulses individually during the mechanical decay. With the above shown value for Δ, mode 2 is not affected by the pulse sent to the AOM at $\omega_{\mathrm{AOM},1}$ within detection sensitivity, while the measured effect of the pulse at $\omega_{\mathrm{AOM},2}$ on mode 1 agrees well with the theoretically predicted optomechanical effect from the light fields at ω_{L2}.

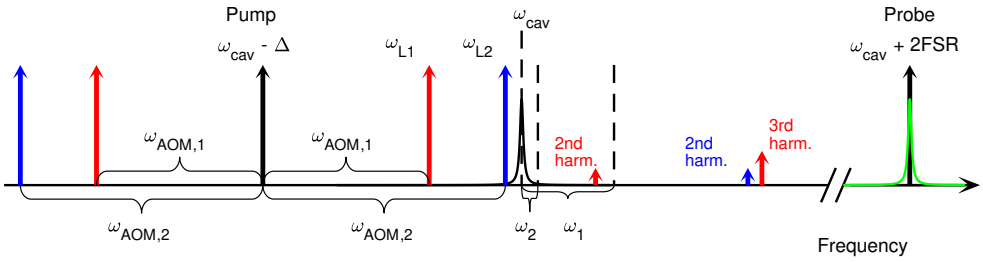

Figure 3.5: Scheme of the optical frequencies. The probe laser is locked to the cavity resonance at $\omega_{\mathrm{cav}} + 2\mathrm{FSR}$. The amplitude of the pump laser at $\omega_{\mathrm{cav}} - \Delta$ is fully modulated by an AOM driven with AC voltage at $\omega_{\mathrm{AOM},i}$, thus only the light fields at $\omega_{\mathrm{pump}} \pm \omega_{\mathrm{AOM},i}$ reach the cavity. The upper sidebands ($\omega_{\mathrm{pump}} + \omega_{\mathrm{AOM},i}$) drive the state transfer, while the unwanted light fields at $\omega_{\mathrm{pump}} - \omega_{\mathrm{AOM},i}$ have a negligible effect due to their large detuning. The nonlinear response of the AOM leads to harmonics (small red and blue arrows) which we measure to also have a negligible effect.

3.2.5 Calibration procedure

The transfer efficiency is defined as the ratio of the phonon population in mode 2 at the end of the transfer process to the phonon population in mode 1 at the beginning. The number of phonons in a mechanical mode $\langle \hat{b}_i^\dagger \hat{b}_i \rangle + \frac{1}{2} \propto u_i^2 \propto R_i^2$, where u_i is the amplitude of oscillation, and R_i is the amplitude of the demodulated reflection signal measured at $\omega_i + \omega_{\mathrm{EOM}}$. Thus the transfer efficiency is

$$\mathrm{Eff}_{1\to 2} = \frac{k_2 R_2^2(t_{end,1\to 2})}{k_1 R_1^2(t_{beginning,1\to 2})}, \tag{3.4}$$

where the state is transferred from mode 1 to mode 2 and k_i are coefficients of proportionality. Let us consider the reverse transfer $2 \to 1$. The product of the transfer

efficiencies

$$\mathrm{Eff}_{1\to2}\mathrm{Eff}_{2\to1} = \frac{R_2^2(t_{end,1\to2})}{R_1^2(t_{beginning,1\to2})}\frac{R_1^2(t_{end,2\to1})}{R_2^2(t_{beginning,2\to1})} \tag{3.5}$$

does not have any coefficients of proportionality, thus it can be measured directly without any calibration. For the parameters of the transfer $\sigma = 25$ ms and $\Delta t/\sigma = 1.25$, this product is measured to be 0.73 ± 0.05. This implies that we demonstrate a transfer efficiency of at least $\sqrt{\mathrm{Eff}_{1\to2}\mathrm{Eff}_{2\to1}} = 0.855 \pm 0.03$, independently of the model and calibrations. A numerical solution of the full model shows that for the above chosen σ and Δt, the efficiencies $\mathrm{Eff}_{1\to2}$ and $\mathrm{Eff}_{2\to1}$ differ by 0.01, which amounts to the transfer efficiency from the defect mode to the 3,3 mode being 0.86 ± 0.03, see Fig. 3.6.

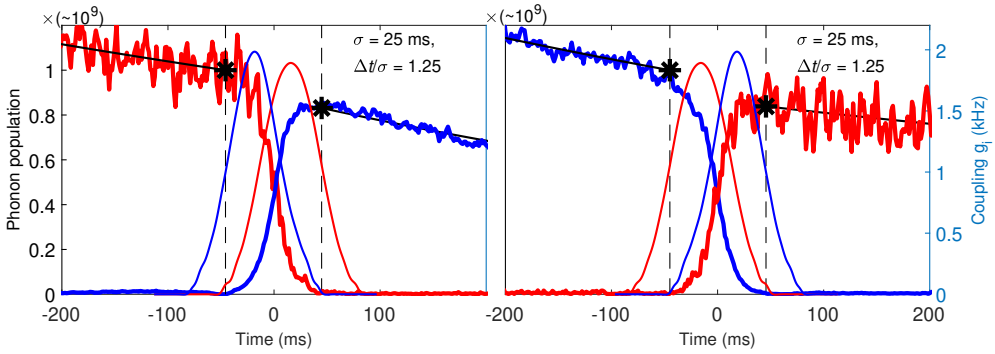

Figure 3.6: Representative single runs of state transfer from mode 1 to mode 2 (left) and in the opposite direction (right). Left scale, thick lines: phonon population as a function of time, red line corresponds to mode 1, blue line to mode 2, both divided by the phonon population of mode 1 in the beginning of the transfer. Right scale, thin lines: multiphoton optomechanical couplings $g_1(t)$ red line, $g_2(t)$ blue line. The driving field pulses have a nearly Gaussian temporal profile, but their beginning and ending are modified such that they have zero amplitude outside the pulse. Vertical lines indicate the beginning and ending of the transfer process. Black stars correspond to the phonon populations used to calculate the transfer efficiency.

The AOM used to shape the driving pulses has a non-linear intensity vs voltage response, which causes the actual temporal profile of the pulse's intensity to deviate from a Gaussian shape. Another consequence of this non-linearity is that the sum of intensities of individual pulses is not equal to the intensity of the pulse resulting from two Gaussian pulses being added and sent to the AOM. To account for these undesired effects, we measured the time profiles of the multiphoton optomechanical coupling $g_i(t)$ as follows. We excite mode 1 to a level much higher than the thermal occupation. During the mechanical decay, we send a single short Gaussian pulse $g_1(t, \sigma)$ to the cavity, with frequency $\omega_{\mathrm{L}1}$ and the same peak intensity as used for the STIRAP measurements. We adjust σ for this pulse so that exactly half of the initial excitation energy is lost due to the optomechanical damping. This gives $\sigma_{1,1/2} = 0.12 \pm 0.01$ ms. Numerical solution of Eq. (3.3) for such a pulse gives the peak value of the pulse $\max g_1(t) \sim 2$ kHz. Next a similar procedure is followed for mode 2,

but σ of the pulse is set equal to $\sigma_{1,1/2}$, and the peak value of the pulse is set so that exactly half of the initial excitation of mode 2 is lost after the pulse $g_2(t, \sigma_{1,1/2})$ at ω_{L2}. This gives the estimate of $\max g_2(t) \sim 2\,\mathrm{kHz}$ and the required voltage amplitude sent to AOM in the pulse.

To get the actual temporal profile of $g_i(t)$, we measure in transmission the time profiles of the intensities of the pulses used for the transfer, with $\sigma = 25\,\mathrm{ms}$ and with each value of $\Delta t/\sigma$ used for the measurements (-1, -0.75, -0.5, .., 3.5, 3.75, 4). In order to measure the exact temporal intensity profile of both STIRAP pulses individually, while both pulses are simultaneously applied (STIRAP sequence), the pump laser detuning Δ is adjusted such that $\omega_{\mathrm{cav}} - \omega_{\mathrm{L1}} \sim \kappa$, while $\omega_{\mathrm{L2}} + \omega_2 = \omega_{\mathrm{L1}} + \omega_1$ as always, making $|\omega_{\mathrm{cav}} - \omega_{\mathrm{L2}}| \gg \kappa$. Therefore the transmitted light consists almost exclusively of the intensity at ω_{L1}. To correct for the small fraction of light at ω_{L2}, we send this pulse individually with the same detunings, and subtract the measured transmission from the case when both pulses are present. We follow the same procedure in order to measure the individual intensity of light at ω_{L2}. The measured intensity profiles of the pulses are used in the numerical simulations presented here.

3.3 Theory

Here we derive Eq. (3.3) and the full model which accounts for the unmatched sidebands. We start from the optomechanical equations of motion [9] in the presence of two mechanical modes $\hat{b}_i$ and two coherent driving fields at ω_{L1} and ω_{L2} with the condition $\omega_{\mathrm{L1}} + \omega_1 = \omega_{\mathrm{L2}} + \omega_2 = \omega_{\mathrm{cav}}$, where ω_i is the frequency of mechanical mode i, i=1,2. In the linearized approximation and in the frame rotating at ω_{cav}, the total intracavity light fields $\hat{a}$ is

$$\hat{a} = |\bar{\alpha}_1(t)|e^{i(\omega_1 t + \phi_1)} + |\bar{\alpha}_2(t)|e^{i(\omega_2 t + \phi_2)} + \delta\hat{a}, \tag{3.6}$$

where $\bar{\alpha}_i$ is the amplitude of the intracavity field due to driving field i, ϕ_i is a constant and $\delta\hat{a}$ is a fluctuating term. The evolution of $\delta\hat{a}$ is given by

$$\delta\dot{\hat{a}} = -\frac{\kappa}{2}\delta\hat{a} + i(G_1\hat{x}_1 + G_2\hat{x}_2)\hat{a}, \tag{3.7}$$

where G_i is the optical frequency shift per displacement of the mechanical mode $\hat{x}_i = x_{zpm,i}(\hat{b}_i + \hat{b}_i^\dagger)$ with x_{zpm} being the zero-point motion of mode i. Neglecting the thermal occupation of the environment, the mechanical modes evolve as

$$\dot{\hat{b}}_i = (-\frac{\Gamma_i}{2} - i\omega_i)\hat{b}_i + ig_{0i}\hat{a}^\dagger\hat{a}, \tag{3.8}$$

where g_{0i} is the single photon optomechanical coupling of mode i. In the frame rotating at ω_i for both mechanical modes $\hat{c}_i = e^{i(\omega_i t + \phi_i)}\hat{b}_i$

$$\dot{\hat{c}}_i = -\frac{\Gamma_i}{2}\hat{c}_i + ig_{0i}\hat{a}^\dagger\hat{a}e^{i(\omega_i t + \phi_i)}. \tag{3.9}$$

The sidebands at ω_{cav} have much larger amplitude than the other sidebands. Thus RWA is a good approximation for this situation. Applying RWA and linearizing, we

obtain

$$\begin{aligned}\hat{a}^\dagger\hat{a}e^{i(\omega_i t+\phi_i)} &= (|\bar{\alpha}_1|e^{-i(\omega_1 t+\phi_1)} + |\bar{\alpha}_2|e^{-i(\omega_2 t+\phi_2)} + \delta\hat{a}^\dagger)\times \\ &\times (|\bar{\alpha}_1|e^{i(\omega_1 t+\phi_1)} + |\bar{\alpha}_2(t)|e^{i(\omega_2 t+\phi_2)} + \delta\hat{a})e^{i(\omega_i t+\phi_i)} = \\ &= |\bar{\alpha}_i|\delta\hat{a},\end{aligned}$$

$$\dot{\hat{c}}_i = -\frac{\Gamma_i}{2}\hat{c}_i + ig_{0i}|\bar{\alpha}_i|\delta\hat{a}, \tag{3.10}$$

$$\delta\dot{\hat{a}} = -\frac{\kappa}{2}\delta\hat{a} + iG_1 x_{zpm,1}|\bar{\alpha}_1|\hat{c}_1 + iG_2 x_{zpm,2}|\bar{\alpha}_2|\hat{c}_2. \tag{3.11}$$

Using the multiphoton optomechanical coupling $g_i(t) = G_i x_{zpm,i}|\bar{\alpha}_i(t)|$, changing notation $\hat{c} \to \hat{b}$ and $\delta\hat{a} \to -\delta\hat{a}$ we get Eq. (3.3):

$$i\dot{\hat{b}}_i = -i\frac{\Gamma_i}{2}\hat{b}_i + g_i(t)\delta\hat{a}, \tag{3.12}$$

$$i\delta\dot{\hat{a}} = -i\frac{\kappa}{2}\delta\hat{a} + g_1(t)\hat{b}_1 + g_2(t)\hat{b}_2. \tag{3.13}$$

Next, we consider the full model which includes the unmatched sidebands by not using RWA. We start with the linearized equation for the light fields Eq. (3.11) and the expression $\hat{x}_i = x_{zpm,i}(\hat{b}_i + \hat{b}_i^\dagger)$. Using Eq. (3.10) we get

$$\begin{aligned}\delta\dot{\hat{a}} = -\frac{\kappa}{2}\delta\hat{a} + i(g_{01}(\hat{b}_1 + \hat{b}_1^\dagger) + g_{02}(\hat{b}_2 + \hat{b}_2^\dagger))\times \\ \times (|\bar{\alpha}_1(t)|e^{i(\omega_1 t+\phi_1)} + |\bar{\alpha}_2(t)|e^{i(\omega_2 t+\phi_2)}).\end{aligned} \tag{3.14}$$

The dynamics of the mechanical modes is still described by Eq. (3.12). As before we change the frame by applying the transformation $\hat{c}_i = e^{i(\omega_i t+\phi_i)}\hat{b}_i$. In the expansion of its last term $ig_{0i}\hat{a}^\dagger\hat{a}$ the terms not including $\delta\hat{a}$ can be omitted and we get

$$\begin{aligned}\dot{\hat{c}}_i = -\frac{\Gamma_i}{2}\hat{c}_i + ig_{0i}e^{i(\omega_i t+\phi_i)}\times \\ \times (|\bar{\alpha}_1(t)|e^{-i(\omega_1 t+\phi_1)}\delta\hat{a} + |\bar{\alpha}_2(t)|e^{-i(\omega_2 t+\phi_2)}\delta\hat{a} + \\ + |\bar{\alpha}_1(t)|e^{i(\omega_1 t+\phi_1)}\delta\hat{a}^\dagger + |\bar{\alpha}_2(t)|e^{i(\omega_2 t+\phi_2)}\delta\hat{a}^\dagger).\end{aligned} \tag{3.15}$$

To simulate this model we average the operators $\hat{a}$, $\hat{c}$ to get the classical fields. Simulation of this model for the experimental parameters is done by solving these differential equations.

The transfer efficiencies calculated by the full model start to deviate from ones by Eq. (3.3) by more than 3% for pulses with $\sigma \gtrsim 25$msec. We see negligibly small dependence of the transfer efficiency on $\phi_1 - \phi_2$.

Note, simulations show that using Eq. (3.3) with added corrections due to the optical spring effect of the unmatched sidebands give incorrect result.

3.4 Results

STIRAP with parameters tuned for maximum phonon number state transfer efficiency is shown in Fig. 3.7. The measurement of a typical transfer process has the following sequence: mode 1 is excited to an amplitude much higher than its thermal occupation by applying an AC voltage in resonance with the mechanical frequency to a needle positioned close to the center of the membrane. During its free decay the

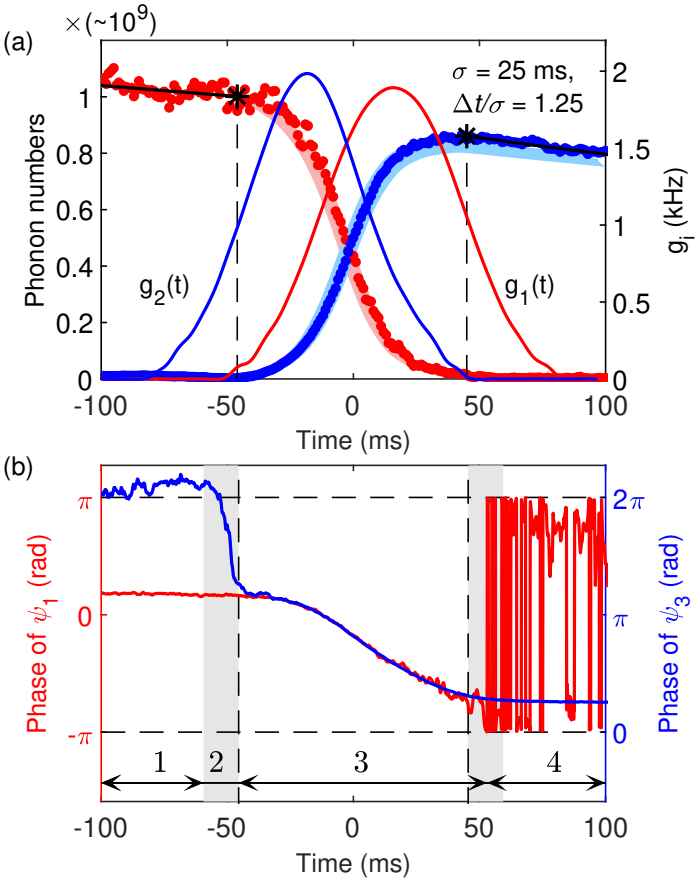

Figure 3.7: Experimental optomechanical STIRAP. (a) Left scale: phonon number as a function of time, red dots correspond to averaged measurements for mode 1 (ψ_1), blue dots for mode 2 (ψ_3). The prefactor 10^9 is a rough estimate. Light red and light blue regions represent the phonon populations with statistical uncertainties (1 standard deviation) obtained from simulations without free fit parameters. Right scale: multiphoton optomechanical coupling strengths, calculated from measured pulse intensities. The driving field pulses have a nearly Gaussian profile with the standard deviation parameter σ and separation Δt, but their beginning and ending are smoothly truncated to zero. Black stars correspond to the phonon populations used to calculate the transfer efficiency (5% of the peak voltage sent to the AOM). (b) Measured phases of mode 1 (red) and mode 2 (blue) in the rotating frame.

two optical pulses are sent which transfers the excitation of mode 1 to mode 2. The transfer starts with the beginning of pulse 1 (red) and finishes with the end of pulse 2 (blue), these moments are denoted by dashed vertical lines. The transfer efficiency is calculated as the ratio of the number of phonons in mechanical mode 2 at the end of the transfer to the number of phonons in mechanical mode 1 at the beginning of the transfer (black stars). A theoretical model without free fit parameters was developed in the classical limit to simulate the transfer process taking into account the corrections due to the other sidebands and the measured profiles of the light pulses (see section Theory), and shows excellent agreement to the experimental data in Fig. 3.7(a). Simulations show that the average rate of loss through the optical mode is $\sim$1 Hz in the dark state during the transfer. We observe small variations in the frequencies of the mechanical modes with each STIRAP sequence. To account for these variations, we measure the mechanical frequencies in thermal motion and adjust the values of the mechanical frequencies for the driving pulse generation accordingly before each STIRAP sequence.

In our realization of STIRAP using coherent state populations, i.e. in the classical regime, the phases of the mechanical modes during the transfer can be continuously monitored, see Fig. 3.7(b). There are four time domains with distinct behavior of phases: in domain 1 $g_1(t) = 0$ and the phase of mode 1 is defined by the excitation used to drive it, while mode 2 is in its thermal motion, thus the difference between the phases is random; in domain 2 STIRAP starts and the phase of mode 2 adjusts itself until the sidebands at $\omega_{\rm cav}$ become π out of phase; in domain 3 the phase of the locked mechanical modes changes due to the optomechanically induced frequency shift from field $\omega_{\rm L2}$ (unmatched sidebands); in domain 4 the read-out signal of mode 1 becomes much less than the read-out noise.

Next we investigate the dependence of the transfer efficiency on the parameters of the process. First the time delay between the optical pulses Δt is varied, see Fig. 3.8. The adiabaticity condition becomes more and more violated when the separation between the pulses is too small or too large, leading to decreasing efficiency. Then the duration of the pulses σ is varied while keeping the time delay Δt optimal. The adiabaticity condition is satisfied increasingly better with longer pulses such that for pulses with $\sigma = 100$ ms only 2% of the initial phonon population in mode 1 is lost through the population and decay of the optical mode. Nevertheless the efficiency starts to decrease for $\sigma \gtrsim 25$ ms due to the mechanical decay of the modes, setting the upper bound on the transfer efficiency. The solid curves in Fig. 3.8(a-b) are numerical results and Fig. 3.8(c-d) compare experiment and simulations for varying Δt and σ. We observe an increasing discrepancy between measured and simulated data for the state transfer with $\sigma \gtrsim 25$ ms. This is caused by membrane heating from the driving pulses and by the defect mode frequency dependence on the amplitude of the full membrane 3,3 mode, see below.

3.4.1 Membrane heating and non-linear effects

We observe increasing discrepancy of measured and simulated data for the state transfer with $\sigma \gtrsim 25$ msec. This is caused by membrane heating by the driving pulses and by the defect mode frequency dependence on the amplitude of the full

membrane 3,3 mode. Driving pulses heat the area of the membrane in the vicinity of the defect which decreases its frequency by $\sim$ 5 Hz (out of 1.25 MHz) through thermal expansion leading to a decrease in the local stress. We observed a frequency change of the defect mode persisting for some time after a driving pulse. The other effect that changes the frequency of the defect mode is non-linearity of the membrane. In the realization of STIRAP, the level of excitation of the 3,3 mode should be

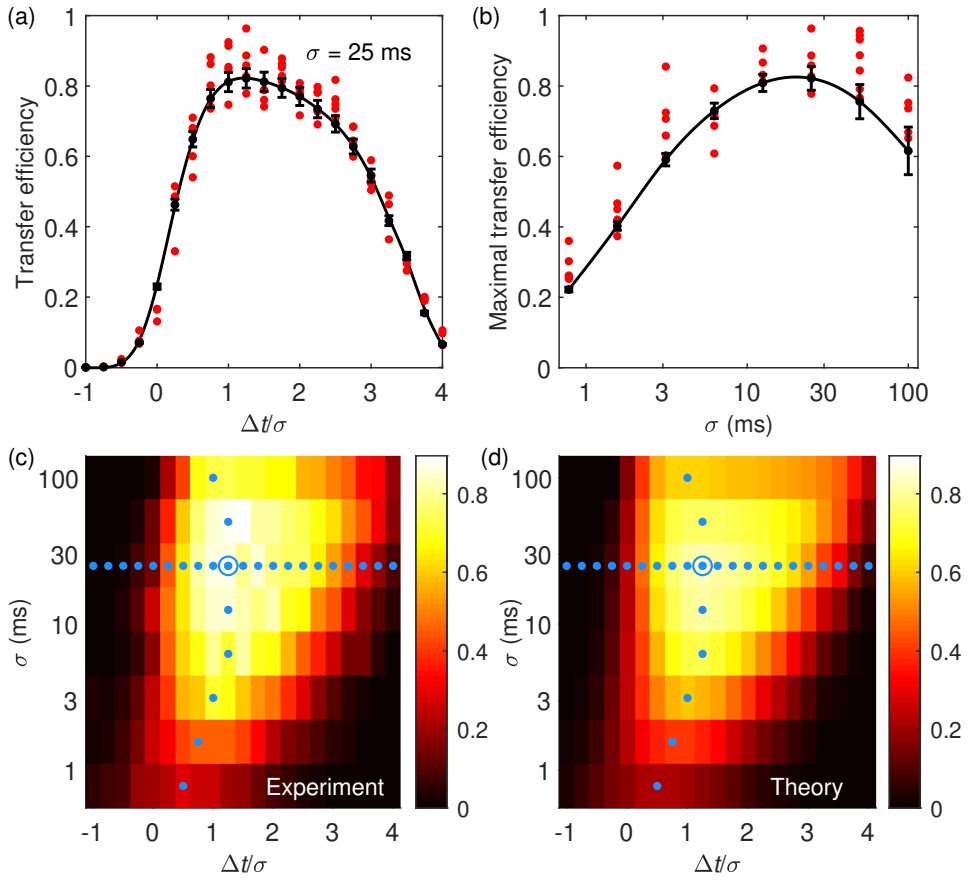

Figure 3.8: The transfer efficiencies under different parameters of the optical pulses. (a) The transfer efficiency as a function of the ratio of the delay between the pulses Δt and the Gaussian pulse width σ. Positive values of Δt correspond to the case that the field at ω_{L2} is applied before the field at ω_{L1}. (b) Maximal transfer efficiencies as a function of σ. In (a) and (b) the red dots show measured efficiencies in individual runs, black dots are the simulated efficiencies, and the black lines are guides to the eye. The increasing error bars for larger σ in (b) are due to observed but not accounted for small non-linear and heating effects. (c) and (d) show the experimental (c) and predicted (d) transfer efficiency as a function of the Gaussian parameter σ and separation Δt. The horizontal row of dots in (c) and (d) correspond to the data shown in (a), while the vertical row of dots correspond to the data shown in (b). The transfer process for the parameters corresponding to the open circle in (c) and (d) is shown in Fig. 3.7.

much higher than its thermal occupation. This requires relatively large amplitudes of the 3,3 mode which effects the frequency of the defect mode through increased stress in the membrane averaged over an oscillation of the 3,3 mode. We observed an increase of the frequency of the defect mode when the 3,3 mode is excited by a couple of Hz.

To calculate ω_{L1} and ω_{L2} we measure the frequencies of the mechanical modes in their thermal motion before each STIRAP sequence. The two effects described above shift the frequency of the defect mode, effectively introducing a small two-photon detuning with complicated dependence on time, which we do not take into account in our simulations. This small two-photon detuning of the order of 5Hz becomes comparable to the width of the two-photon detuning curve and starts influencing the state transfer with $\sigma \gtrsim 25$ msec as the width of the two-photon detuning curve is inversely proportional to σ.

A signature of STIRAP [13] is strong sensitivity of the transfer efficiency to the two-photon detuning $\Delta_{\mathrm{2ph}} = (\omega_{\mathrm{L1}} + \omega_1) - (\omega_{\mathrm{L2}} + \omega_2)$ given $\Delta_{\mathrm{1ph}} = 0$, compared to the sensitivity to the single-photon detuning $\Delta_{\mathrm{1ph}} = \omega_{\mathrm{cav}} - (\omega_{\mathrm{L1}} + \omega_1)$ given $\Delta_{\mathrm{2ph}} = 0$, Fig. 3.9. The frequency scale for the two-photon detuning is set by the duration of the transfer process: $\Delta_{\mathrm{2ph}} \sim \pi/\tau_{\mathrm{transfer}}$, implying that the sidebands at ω_{cav} accumulate a phase difference of π during the transfer and consequently no longer interfere destructively. The frequency scale for Δ_{1ph} is set by the optical cavity linewidth κ: non-zero Δ_{1ph} leads to changes in the intracavity light fields intensities and in the amplitudes of the sidebands.

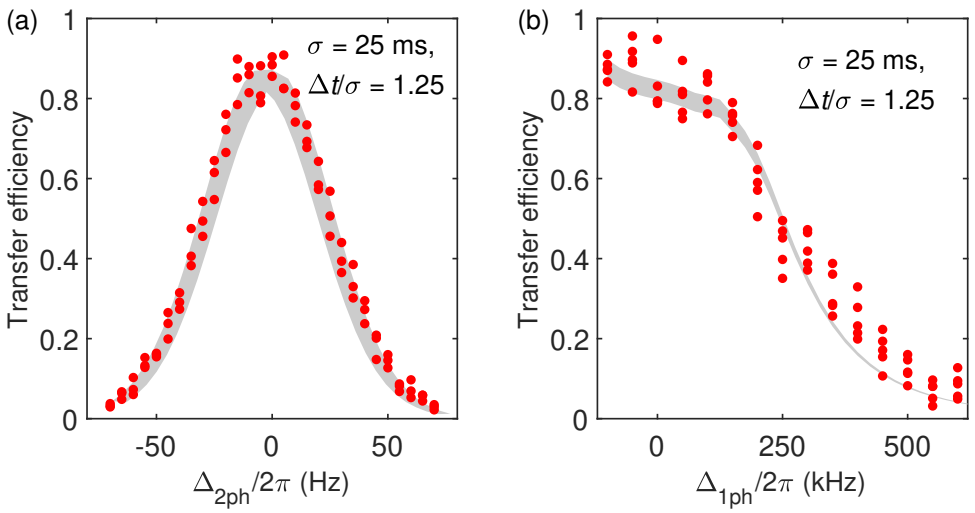

Figure 3.9: (a) The transfer efficiency as a function of the two-photon detuning Δ_{2ph} with zero single-photon detuning. (b) The efficiency as a function of the single-photon detuning Δ_{1ph} with zero two-photon detuning. In (a) and (b) the red circles are measured efficiencies in individual runs, and the shaded regions are simulated efficiencies with statistical uncertainties. The simulated curve in (a) has a frequency correction of 4 Hz caused by small non-linear and heating effects.

The highest phonon number transfer efficiency we observe in our system is $86 \pm 3\%$. The highest demonstrated state transfer efficiencies in other systems are: transmon qubit 83% [38]; Bose–Einstein condensate of atoms 87% [57]; trapped ions 90% [37]; superconducting Xmon qutrit 96% [58]; doped crystals $98 \pm 2\%$ [59]; atom beams $98 \pm 2\%$ [60]. In general, the STIRAP scheme in optomechanics can result in the transfer efficiencies close to unity if the following set of requirements is satisfied:

$$\begin{aligned} &\omega_i \gg \kappa, \\ &|\omega_1 - \omega_2| \gg \kappa, \\ &\kappa \gg \max g_i(t), \\ &\tau \max g_i^2(t) \gg \kappa, \\ &\Gamma_i \tau_{\mathrm{transfer}} \ll 1. \end{aligned} \tag{3.16}$$

The first two inequalities allow to address the mechanical modes individually; the third one is the weak coupling regime; the forth one is the adiabaticity condition; the last inequality assumes that the loss due to intrinsic mechanical decay during the transfer is small. This set of stringent requirements applies both to the classical and the quantum regime of STIRAP in optomechanics. Other experimental challenges are the accurate control of 1- and 2-photon detunings, circumventing detrimental effects of the unmatched sidebands, and proving stable subwavelength positioning of the membrane to maximize the coupling strength.

3.5 Conclusions

Here we have shown the first optomechanical implementation of STIRAP and demonstrated a maximum phonon number state transfer efficiency of $86 \pm 3\%$. The efficiency is benchmarked against variation in the STIRAP pulse duration and separation as well as against the STIRAP single- and 2-photon detuning and is found to be in good agreement with theory. Our quantum simulations show that STIRAP of a single phonon Fock state is feasible to observe with demonstrated technology. Furthermore, modified versions of STIRAP (fractional STIRAP [61], tripod STIRAP [62]) can be used to create and detect entangled mechanical states. Therefore, STIRAP in optomehanics can play an important role in quantum information protocols and in generating macroscopic superposition states.